Development and validation of a 3D computational tool to describe concrete behaviour at mesoscale. Application to the alkali-silica reaction

Isabelle Comby-Peyrot, Fabrice Bernard, Pierre-Olivier Bouchard, François Bay, Eric Garcia-Diaz

▶ **To cite this version:**

Isabelle Comby-Peyrot, Fabrice Bernard, Pierre-Olivier Bouchard, François Bay, Eric Garcia-Diaz. Development and validation of a 3D computational tool to describe concrete behaviour at mesoscale. Application to the alkali-silica reaction. Computational Materials Science, 2009, 46 (4), pp.1163-1177. ⟨10.1016/j.commatsci.2009.06.002⟩. ⟨hal-00508403⟩

HAL Id: hal-00508403

https://minesparis-psl.hal.science/hal-00508403v1

Submitted on 25 Jun 2025

HAL is a multi-disciplinary open access archive for the deposit and dissemination of scientific research documents, whether they are published or not. The documents may come from teaching and research institutions in France or abroad, or from public or private research centers.

L'archive ouverte pluridisciplinaire **HAL**, est destinée au dépôt et à la diffusion de documents scientifiques de niveau recherche, publiés ou non, émanant des établissements d'enseignement et de recherche français ou étrangers, des laboratoires publics ou privés.

HAL Authorization

Development and validation of a 3D computational tool to describe concrete behaviour at mesoscale. Application to the alkali-silica reaction

Isabelle Comby-Peyrot [a,b], Fabrice Bernard [c,*], Pierre-Olivier Bouchard [a], François Bay [a], Eric Garcia-Diaz [b]

[a] Centre de Mise en Forme des Matériaux, Ecole des Mines de Paris UMR 7635 CNRS, BP 207, 06904 Sophia-Antipolis Cedex, France
[b] Ecole des Mines de Douai, Civil and Environmental Engineering Department, 941 rue Charles Bourseul, 59508 Douai Cedex, France
[c] LGCGM, Institut National des Sciences Appliquées, 20 Avenue des Buttes de Coësmes, 35043 Rennes Cedex, France

A B S T R A C T

This paper presents the development and the validation of a 3D numerical tool called "finite element model for concrete analysis method" (FEMCAM). This tool is established to model quasi-brittle and het-erogeneous materials like concrete. This last one is here considered as a 3D biphasic material composed of coarse aggregates embedded in mortar. A particular attention is paid to a realistic generation of par-ticles in concrete sample. A non-local Mazars model is used to reproduce the mortar behaviour. The val-idation of this mesomodelling is performed by comparison with experimental results on various tests (3-point bending tests, compressive tests and "Brazilian" splitting tests). All these results are used to study the mechanical consequences of the alkali-silica reaction, one of the main and most famous chemical degradations of concrete structures such as dams, pavements or bridges. At the mesoscale, this reaction is characterized by a swelling of the reactive granular skeleton.

PACS:
61.72.Qq
62.20.De
62.20.Mm
81.05.Rm
81.70.Bt
82.20.Wt

Keywords:
Concrete
Mortar
Aggregates
Mesolevel modelling
Mesomechanics
Heterogeneous description
Alkali-silica reaction

1. Introduction

Concrete is a complex multi-scale composite with a random microstructure at different length scales ranging from nanometer scale to the macroscopic decimeter scale. From a mesoscopic point of view (for length in between 1 and 10 cm), aggregates with interfacial transition zone (ITZ) embedded in a homogeneous mortar matrix can typically be observed [1].

Recent advances in the modelling of the behaviour of cement-based materials are particularly related with this mesolevel structure. A few numerical models for the simulation of the fracture process at this scale in concrete have been performed in recent years [2–5]. Modelling concrete as a heterogeneous material is particularly interesting in order to:

- estimate and understand local mechanisms of deformation;
- better simulate damage initiation and growth;
- study and compare different concrete formulations; and
- describe accurately chemical degradation involving changes in the microstructure.

The large majority of these modellings has still computational limitations and is most of the time performed in 2D. Besides some important and very physical parameters, such as wall effects and maximum paste thickness (MPT) are not considered. The tremendous increase of computational capabilities enables the development of numerical simulations based on realistic explicit descriptions of the material [6,7].

The aim of this paper is to present the development and the validation of a new 3D mesoscopic modelling of concrete, called finite element model for concrete analysis method (FEMCAM), with assumptions as close as possible to reality and with a very accurate representation of the heterogeneities. This tool is then applied, in

* Corresponding author.
E-mail address: Fabrice.Bernard@insa-rennes.fr (F. Bernard).

the last part of the present article, to a sensitivity study on various parameters (aggregates volume, distribution and maximal diameter) and to the modelling of damage involved by the alkali-silica reaction (ASR).

2. Generation of mesoscopic concrete

2.1. Concrete composition

The concrete modelled in this paper is chosen to be sensitive to the alkali-silica reaction as the study of this chemical degradation is one of the objectives of this work [8].

A portland cement, CEM I 42.5R type, from Heming, supplied by the Obourg corporation, is used. This cement has been chosen because of its high alkaline content which accelerates the ASR development. A non-reactive sand, commonly called sand from "Boulonnais", is used. It is composed of 90% limestone and 7% silica. Two different types of aggregates are considered too. The aggregates from "Boulonnais" (4/20 mm) are composed of non-reactive limestone (98%) whereas the aggregates from "Savreux" (5/20 mm) are extracted from flint shingle and sea sand and are composed of silica (87%) for the main part.

The particle size distribution of the sand and the two different aggregates are presented in Fig. 1. Table 1 presents the whole material formulation. The water-to-cement ratio (W/C) is equal to 0.4. This formulation corresponds to the most reactive formulation for the ASR in terms of amount of free swelling without adding any adjuvant. The high content of cement allows a greater reactivity.

2.2. Discretization of the particle size distribution (psd) and calculation of the whole number of particles

The following calculations are performed knowing the mass content of the various components comprise between two diameters of the particle size distribution and making the assumption that all particles are spherical.

Tables 2 and 3 show the total number of particles present in a common 70 × 70 × 280 mm sample which can be considered as a representative volume element (RVE) of concrete. In Table 2, the choice of the various diameters for the discretization of the aggregates size distribution is based on the experimental determination of the psd following standard EN 933-1. The values presented are the averages of the different sieves used for aggregates (6.3, 8, 10, 12.5, 16 and 20 mm). The too important aggregates number, due to large differences of scale in the systems, does not allow the modelling of such systems as one. Thus, it is necessary to make the assumption of the scales separation and to consider the concrete as a two phases material: some coarse aggregates dispersed in a matrix of mortar. Since in our study, sand and aggregates are perfectly separated (see the presentation of the components in Section 2.1) the choice of the limit between them is easy. Thus 935 aggregates should be generated (Table 2).

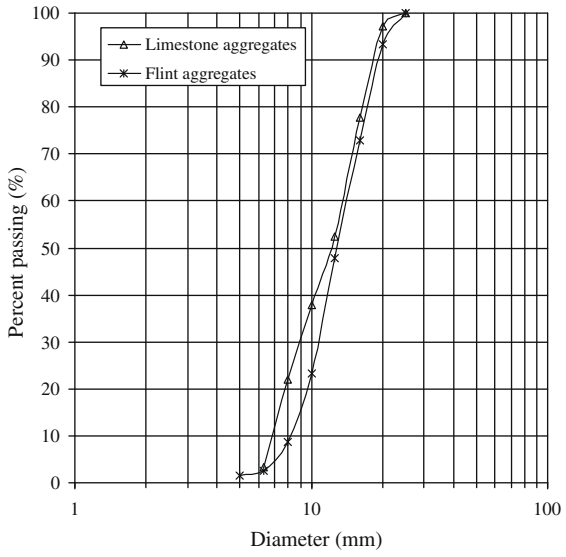

Fig. 1. Size distribution of aggregates.

Table 1
Concrete formulation and corresponding density.

	Composition (kg/m^3)	Density (g/cm^3)
Cement CPA CEM I 42,5 from Heming	500	3.16
Sand(0–4 mm)	552	2.65
Flint aggregates "Savreux"	583	2.6
Limestone aggregates "Boulonnais"	583	2.65
Water	200	

Table 2
Selected grain size distribution with 935 coarse aggregates.

Mean diameter of aggregates (mm)	Aggregates number
18	38
14.25	101
11.25	162
9	244
7.15	389

Table 3
Estimation of the number of sand grains in a 7 × 7 × 28 cm concrete sample.

Mean diameter (mm)	Aggregates number
5	382
4	1005
3.15	1999
2.5	3775
2	7802
1.6	20,319
1.25	25,509
1	63,725
0.8	159,042
0.63	196,486
0.5	427,186
0.4	930,742
0.315	1,408,996
0.25	3,114,430
0.2	6,278,076
0.16	13,846,153
0.125	17,332,478
0.1	43,625,390
Total	87,443,495

2.3. Generation of aggregates particles

2.3.1. Presentation of the software used in the study

The software used in this work is derived from the commercial software Forge3® developed by CEMEF. Forge3® is a process simulation tool based on the finite element method and initially dedicated to the simulation of forming processes such as forging. Forge3® can deal with multimaterial bodies, which is interesting to model concrete at the mesoscopic scale (matrix and aggregates). A completely parallel solver enables faster computations on very fine meshes.

The software is based on a mixed velocity–pressure formulation with linear tetrahedrical elements and a bubble function (mini

element P1+/P1) [9]. The stability condition (Brezzi–Bakuska condition) for this element is ensured by using an additional node for velocity at the center of the element.

2.3.2. Methodology

Mesolevel models require the generation of an aggregate–mortar structure in a realistic way. A "take and place" method [4,10–12] based on a 3D existing mesh is used. This method consists in placing aggregates one by one.

The generation mechanism proposed here should fulfil the following requirements:

- the location of the aggregates particles should be randomly selected;
- the spatial aggregates distribution should be relatively uniform;
- the grain size distribution and aggregates content should be exactly matched; and
- some physical aspects like maximum paste thickness and edge effects [13] should be taken into account.

The grain size and aggregates content are provided by the particle size distribution. A histogram of five classes is considered as explained in Section 2.2. The maximum paste thickness is the mean distance between two coarse aggregates which are in contact during the dry stacking of the material. After the setting of the cement, these aggregates are surrounded by a paste layer. This distance acts then like a distance of exclusion between the largest aggregates [13]. The thickness of the paste, noted "l" here, is proportional to the aggregate diameter as follows [14]:

$$l = d_{\max}\left(\sqrt[3]{\frac{g^*}{g}} - 1\right) \tag{1}$$

where $d_{\max}$ is the maximum size of aggregates, g is the aggregates volume in a concrete sample, and g^* is the maximum aggregates concentration (see Fig. 2).

De Larrard [13] gives different formula to calculate g^* depending on aggregates shape. For example, for rolled grains:

$$g^* = 1 - 0.47\left(\frac{d_{\min}}{d_{\max}}\right)^{0.22} \tag{2}$$

where $d_{\min}$ is the minimum size of aggregates.

The edge effect implies that aggregates content is less important near to the faces of a concrete sample. If V_P is the volume located between the edge and the distance $d/2$, where d is the considered aggregate diameter, the compactness in V_P is lower than the compactness α in the center of the sample (see Fig. 3). The mean compactness $\bar{\alpha}$ in the whole volume is equal to [13]:

$$\bar{\alpha} = (1 - V_P)\alpha + V_P k_w \alpha \tag{3}$$

with $k_w = 0.88$ for rolled aggregates and $k_w = 0.77$ for crushed aggregates.

This formula enables to know how aggregates are generated for each aggregates size in the volume V_P.

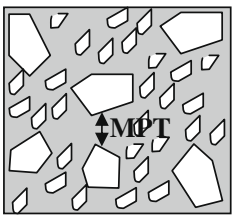

Fig. 2. Concrete defined as a dry stacking injected with the mortar paste. Definition of MPT.

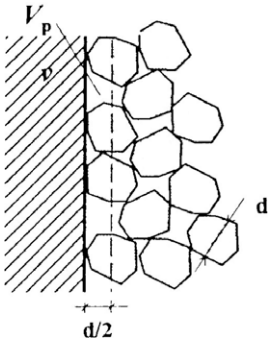

Fig. 3. Wall attachment effect on a stacking of grains of unique size (from [11]).

2.3.3. Algorithm

An algorithm has been implemented in the FE code used in this study. Aggregates are considered as a sphere with a radius R given by the grain size distribution. Starting from the largest ones, aggregates are sequentially placed into the mortar paste. The allocation of the particles consists in finding suitable values for the center-point coordinates. The word "suitable" refers to the four important requirements i.e. the particles should not overlap each other, should be entirely inside the specimen and fairly uniformly distributed. Besides edge effects and exclusion distance for the largest aggregates should be considered. It is also important to have no contact between aggregates (nodes in common) in the skeleton. Indeed such a perfect contact would not be conform to reality. Then, when a node is chosen for the center-point of an aggregate, all elements comprised in a sphere with a radius equal to the sum of the aggregate radius and the MPT (if necessary) are detected as well as all the phases to which they belong. If one of the elements belongs to an aggregate, the point is not suitable and another location is chosen and studied in the same way.

The generation of the aggregates stops when the number of aggregates to generate is reached or when the volume of the aggregate skeleton is also reached.

Fig. 4 details the random algorithm for aggregates generation. When the algorithm does not succeed to find a suitable position for an aggregate, it continues with a smaller one. Thus the accuracy of the algorithm is related to the differences between the real and the computational particle size distributions.

Fig. 5a shows a heterogeneous $70 \times 70 \times 280$ mm sample generated in this study. The mesh size is about 2 mm. This presented mesh contains 165,669 nodes and 902,826 elements. It corresponds to the limit of the generation of a mesh using a standard computer (Intel Xeon Machine 1.7 GHz, 512 Mo RAM). The CPU time needed to generate this skeleton is about 1 h.

As a "take and place" method is used, this aggregates generation is mesh-dependant. A very fine mesh allows to obtain a result closer to the desired grain size distribution. On the contrary, the consequences of a coarse mesh are the obtaining of a sample with grains size values far away from the desired initial sizes. Besides fine meshes favour smooth particles whereas coarse meshes imply rough particles. Fig. 5b shows a zoom on an aggregate of the sample. This numerical aggregate does not have a very regular shape since it depends on the mesh structure. Then aggregates are not perfectly spherical, which is closer to reality. Then it can be concluded that the algorithm generates a realistic granular skeleton in comparison with real aggregates.

It can also be noted that a mesh size equal to 2 mm (finest mesh up to now for a $70 \times 70 \times 280$ mm sample) is several times higher than typical interfacial transition zone thickness (of the order of 20 μm). Because of the large differences of scale in the system, it is impossible to take into account explicitly the ITZ.

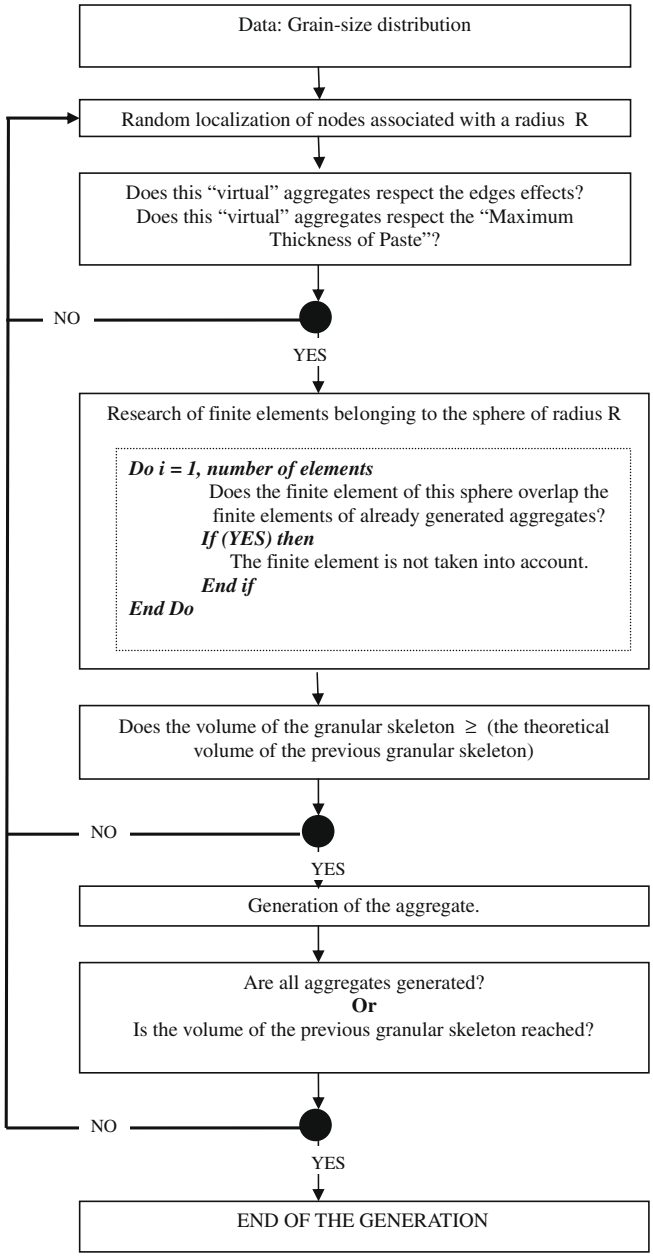

Fig. 4. Random algorithm of aggregates generation.

In order to simplify the calculation, the contact between aggregates and mortar is considered as bilateral sticking (no sliding and no decohesion between mortar and aggregates).

3. Modelling behaviour at mesoscale

3.1. Constitutive laws of the various components

The properties of both aggregates and cement paste are considered. In a first approach, aggregates are assumed to be purely elastic. Mortar is assumed to be an elastic damage material. The non-local version of the Mazars model is used [15,16]. This method aims at modelling the modification of the material elastic behaviour with a scalar damage variable which affects stiffness. This variable, noted D, is the damage indicator. D includes damage due to both compression and tension; its value varies from 0 (for uncracked material) to 1 (for macro-cracked material). The variation of D is governed by the equivalent strain $\tilde{\varepsilon}$ [15,17].

$$\tilde{\varepsilon} = \sqrt{\sum_{i=1}^{3} \langle \varepsilon_i \rangle_+^2} \tag{4}$$

where $\langle \ldots \rangle_+$ denotes the positive part $\left(\langle \varepsilon_i \rangle_+ = \left(\frac{\varepsilon_i + |\varepsilon_i|}{2} \right) \right)$ and $(\varepsilon_i)_{i\in[1,3]}$ the principal strain components.

An evolutive damage threshold K is introduced depending on the variable D. For a given damage state, the form of the loading function is given by:

$$f(\varepsilon, D) = \tilde{\varepsilon} - K(D) \tag{5}$$

The growth of damage is obtained when the equivalent strain reaches the threshold K initialized at ε_{D_0}:

$$\text{If} \quad f(\varepsilon, D) = \tilde{\varepsilon} - K = 0 \quad \text{then} \begin{cases} D = D(K) \\ K = \tilde{\varepsilon} \end{cases} \tag{6}$$

The damage scalar D is calculated through the damage indicators in tension (D_T) and in compression (D_C):

$$D = \alpha_T^{\beta} D_T + (1 - \alpha_T)^{\beta} D_C \tag{7}$$

The parameter β acts on the shear response of the material. It is usually considered to be constant equal to 1.05. The weight α_T is defined such as:

$$\alpha_T = \sum_{i=1}^{3} \frac{\langle \varepsilon_i \rangle_+ \varepsilon_i}{\tilde{\varepsilon}^2} \tag{8}$$

Damage evolution is given by:

$$D_{T,C} = 1 - \frac{\varepsilon_{D_0}(1 - A_{T,C})}{\tilde{\varepsilon}} - \frac{A_{T,C}}{\exp\left[B_{T,C}(\tilde{\varepsilon} - \varepsilon_{D_0})\right]} \tag{9}$$

$A_{T,C}$ and $B_{T,C}$ as well as ε_{D_0} are material parameters.

The initial model induces localization and discontinuity in the displacement field and then needs improvements. Wriggers and Moftah [6] mentioned that non-local approaches should be used in future computations in order to limit strain localization and to

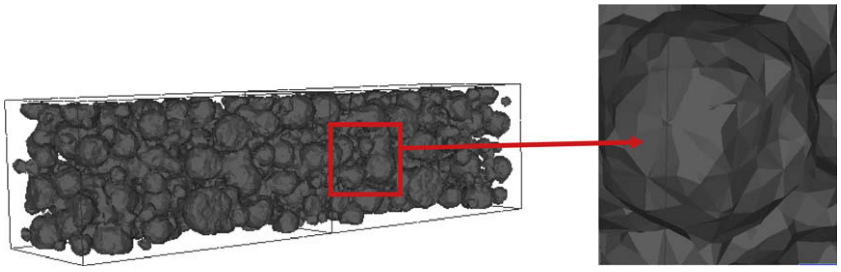

Fig. 5. (a) Heterogeneous sample generated in FEMCAM. (b) Zoom on an aggregate in the sample.

circumvent mesh sensitivity associated with strain softening. In this work a gradient based formulation is used with an implicit formulation [18]. Compared to non-local models, this approach is better-adapted to heterogeneous materials since the evaluation of the non-local equivalent strain at a point, $\bar{\varepsilon}$, is independent of the behaviour of the neighbouring elements. Thus the non-local equivalent strain is the solution of the boundary value problem:

$$\begin{cases} \tilde{\varepsilon} - \tilde{c}\nabla^2\tilde{\varepsilon} = \bar{\varepsilon} \\ \frac{\partial\tilde{\varepsilon}}{\partial\vec{n}} = 0 \end{cases} \tag{10}$$

where $\vec{n}$ denotes the external normal unit vector.

Jason [19] has carried out a numerical campaign where he has compared load–displacement curves on three points bending tests between the results obtained with an integral non-local model and a gradient approach. He has found:

$$\tilde{c} \approx \frac{9d_{\max}^2}{16} \tag{11}$$

where $d_{\max}$ is the maximum size of aggregates.

$\bar{\varepsilon}$ replaces $\tilde{\varepsilon}$ in the definition of the loading surface f.

The implementation of this model in the specific FE software used in this study, which has the particularity to have a mixed velocity–pressure formulation, is well described in a previous publication of the authors [20].

In order to model concrete failure an "kill element" method is used: when the non-local equivalent strain $\bar{\varepsilon}$ reaches in an element a critical value, noted $\bar{\varepsilon}^{\text{crit}}$, the element mechanical contribution to the stiffness is set to zero and the element is removed from the mesh. $\bar{\varepsilon}^{\text{crit}}$ represents the equivalent strain beyond which macrocracks are initiated. This method is necessary to reproduce the brittleness of the material (probably due to the high cement content) and also to avoid any convergence problems due to the excessive distortion of elements that can no longer carry stresses.

Table 4
Parameters to identify.

Parameters to identify	Meaning
E_{mortar}	Young modulus of the mortar paste of concrete
ν_{mortar}	Poisson ratio of the mortar paste of concrete
$E_{\text{aggregate}}$	Young modulus of the aggregates
$\nu_{\text{aggregate}}$	Poisson ratio of the aggregates
A_C	Related to damage evolution in compression
B_C	Related to damage evolution in compression
A_T	Related to damage evolution in tension
B_T	Related to damage evolution in tension
ε_{D_0}	Damage threshold
$\tilde{\varepsilon}_T^{\text{crit}}, \tilde{\varepsilon}_C^{\text{crit}}$	Fracture threshold
$\tilde{c}$	Non-local model parameter

3.2. Identification of the model material parameters

A fine simulation requires material parameters to be determined with a great accuracy. Then the parameters of the elastic behaviour for both mortar and aggregates as well as the parameters of the damage behaviour need to be identified. Table 4 summarizes these various parameters. The determination is performed by means of inverse analysis on experimental tests. Compression and 3-point bending tests have been carried out on 7 days maturated samples. All these samples have been stored in water in a temperature regulated room.

3.2.1. Inverse analysis program

An inverse analysis tool, called "RheoConcrete" has been developed in this study. The identification process enables to find a good approximation of the numerical values. It is based on experimental data which are compared to numerical ones. At each simulation a criterion is used to estimate if it is necessary to improve the numerical parameters accuracy. Fig. 6 summarizes the procedure. The minimization is performed by means of an evolution algorithm [21]. Such an algorithm is inherently parallel and enables to treat simultaneously several individuals. This method is more robust than common determinist approaches.

3.2.2. First strategy of parameters identification and modelling validation

3.2.2.1. Parameters identification on mortar sample. The first approach consists in identifying the model parameters by means of experimental tests carried out on mortar samples. As previously explained, 3-point bending tests and compression tests have been performed. Compression tests are led on $\phi 11 \times h22$ cm wet cylindrical sample instrumented with four strain gages (two longitudinal gages and two rosettes). Only the locations of the gages are dried to avoid any disbonding. Besides displacement measurements are made using three LVDT sensors settled every 60° at the exterior of the sample. Cylindrical samples are also polished and capped with sulphur to obtain parallel faces. The used testing machine, of type INSTRON 8500, has a loading capacity of 1000 kN. Loading is conducted using displacement control with a closed-loop system in order to maintain a uniform rate of loading. Data

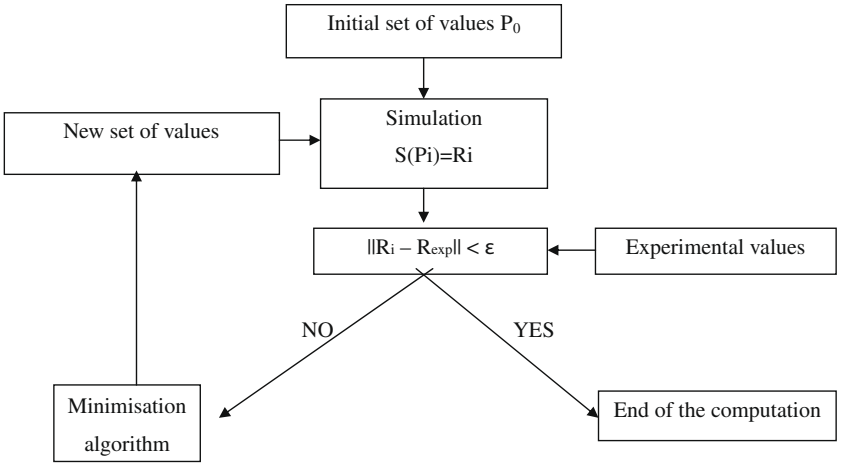

Fig. 6. Inverse analysis modulus.

are collected thanks to an acquisition system (5110, Vishay). Tests are carried out until complete failure. Three different samples are tested. Load–displacement curves as well as stress–strain relationships are systematically recorded. The very brittle behaviour is probably due to the high cement content.

3-Point bending tests are performed on $40 \times 40 \times 160$ mm wet parallelepipedic sample instrumented with a longitudinal strain gage glued on the bottom face. Only the locations of the gages are dried. A displacement sensor is also placed to measure the deflection of the sample. The testing machine used for such tests is of type INSTRON 8505 and it has a loading capacity equal to 150 kN. The loading is conducted using displacement control and led until failure. Three different samples are also tested and load–deflection curves are systematically recorded.

In order to determine the parameters of the Mazars model for mortar, simulations of previous experiments are led on homogeneous material. The inverse analysis modulus enables to compare experimental and numerical curves in order to determine model parameters. Considering that the larger grains for mortar are 5 mm diameter, the $\tilde{c}$ value is set to 15 mm^2 (see Eq. (11)). Table 5 gives the values of the different parameters identified on compression tests. The CPU time required to identify these parameters is about 5 h. It corresponds to an error of 8.1×10^{-5}.

Fig. 7 presents experimental and numerical load–displacement curves for compression tests.

3.2.2.2. Validation of the modelling on concrete sample. In order to validate the mesoscale modelling an experimental campaign has been set up on concrete sample. As for mortar, compression and 3-point bending tests have been performed with the same instrumentation. The dimensions of the tested sample are 16×32 and $7 \times 7 \times 28$ cm, respectively, for compression and 3-point bending tests.

Table 5
Damage identification of mortar parameters in compression (from experiments on mortar).

E_{mortar} (GPa)	20.8
ν_{mortar}	0.2
A_C	1.27879
B_C	457.085
ε_{D_0}	3×10^{-5}
$\tilde{\varepsilon}_C^{\text{crit}}$	1.52×10^{-3}

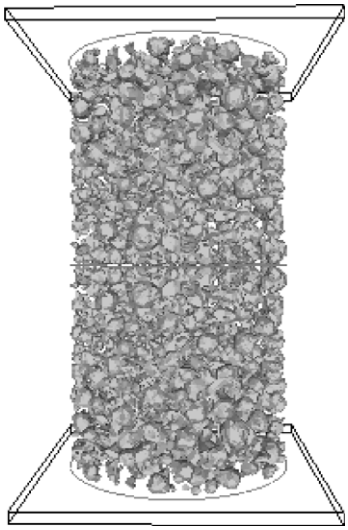

Fig. 8. Heterogeneous aspect of the cylindrical sample: 46,987 nodes and 250,033 elements.

Fig. 8 shows the heterogeneous aspect of the mesh used for the modelling of compressive tests. Table 6 presents the particle size distribution: 2978 aggregates are generated in the numerical concrete sample. Heterogenous meshed sample for 3-point bending test has already been shown in Section 2.3 (Fig. 5).

The modelling of the tests has also been performed with model parameters identified on mortar samples. Classical values of Young's modulus and Poisson coefficient issued from the literature are considered for aggregates: $E_{\text{aggregate}} = 70$ GPa and $\nu_{\text{aggregate}} = 0.2$.

Fig. 9 shows the comparison between experimental and numerical stress–strain compression curves. Large differences are observed: the numerical compression strength is about 55 MPa whereas the experimental strength reaches only 34 MPa. Damage effects are underestimated. It means that damage parameters are well identified on mortar but do not represent the physical behaviour of the mortar paste.

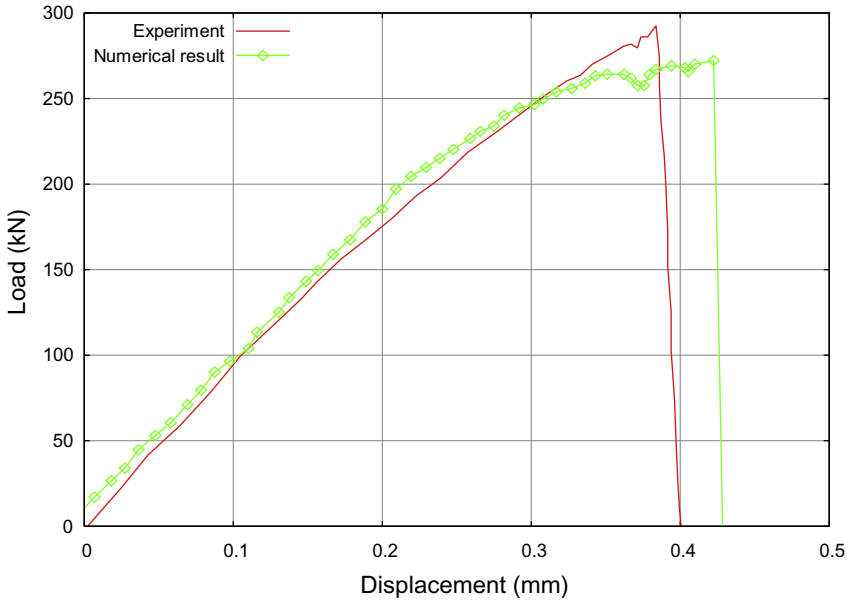

Fig. 7. Load–displacement curves for a compressive test on mortar sample.

Table 6
Particle size distribution with 2978 coarse aggregates (for 16×32 cylindrical sample).

Mean diameter (mm)	Aggregates number
22.5	40
18	294
14.25	502
11.25	428
9	604
7.25	1110
Total	2978

Table 7
Damage identification of mortar parameters (from experiments on concrete).

E_{mortar} (GPa)	18.69
ν_{mortar}	0.2
A_C	1.012
B_C	657.08
A_T	1.18
B_T	50000
ε_{D_0}	9.1×10^{-5}
$\tilde{\varepsilon}_C^{\text{crit}}$	8.72×10^{-4}
$\tilde{\varepsilon}_T^{\text{crit}}$	1.63×10^{-4}

3.2.3. Discussion on the first strategy

The analysis of these results shows that this first approach is not well adapted to model concrete. It shows that it is impossible to consider the mortar paste of concrete with the same mechanical behaviour as mortar alone. Dupray et al. [7] arrived to the same conclusions. Several hypotheses can be formulated to explain this result:

- formation of microcracks due to a shrinkage phenomenon (especially autogenous shrinkage since all the samples are stored in water). These microcracks appear because of restrained deformations due to the presence of coarse aggregates [22]. This phenomenon is probably more important and dispersed for concrete than for mortar;
- creation of an interfacial transition zone between aggregates and mortar paste. By identifying the mortar paste (of concrete) with mortar alone, the mechanical effect of the ITZ is not considered. Akçaoglu et al. [23] explain that this phase has little influence on the peak value. However it can play an important role on damage evolution;
- creation of voids inside the material due to the mixing of the constituents; and
- perfect contact between the aggregates and mortar paste which can be questionable.

All these reasons lead to non-negligible limitations on the multi-scale approaches to describe concrete behaviour and more especially on the up-scaling between mortar and concrete. On the contrary, the transition between paste and mortar has been successfully performed in [24]. In these methods, the outcomes at a lower scale are used as entry data at an upper scale.

3.2.4. Second strategy of parameters identification and modelling validation

3.2.4.1. Parameters identification on concrete samples. In this approach Mazars parameters are identified on previous experiments led on concrete samples. ITZ, and supplementary voids or microcracks are thus indirectly taken into account through a homogeneous behaviour of the mortar inside concrete. Young's modulus and Poisson coefficient of aggregates are, respectively, 70 GPa and 0.2. $\tilde{c}$ is taken equal to 15 mm^2 as previously. The identification is as follows:

- generation of a 16×32 cm cylindrical heterogeneous sample;
- identification of the elastic parameters on compression tests;
- generation of $7 \times 7 \times 28$ cm prismatic heterogeneous sample;
- identification of damage parameters in compression on uniaxial compressive tests; and
- identification of damage parameters in tension thanks to results on 3-point bending tests.

The meshes used in this section are those presented in Figs. 5 and 8.

Table 7 gives the best values of the various parameters for mortar behaviour identified thanks to the inverse analysis modulus RheoConcrete.

Figs. 10 and 11 present, respectively, comparisons of numerical and experimental load–displacement curves obtained for 3-point bending test and compression test on concrete.

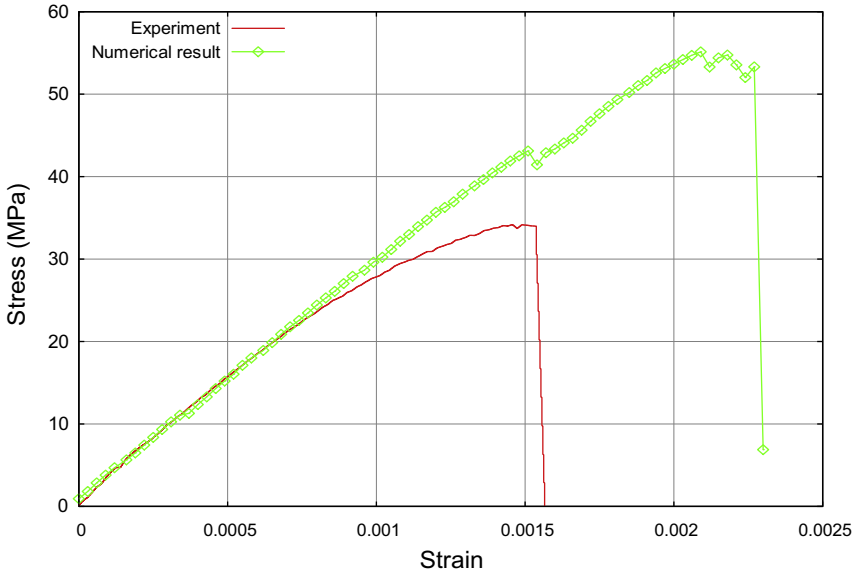

Fig. 9. Comparison of the experimental and numerical stress–strain curves for a compression test on concrete.

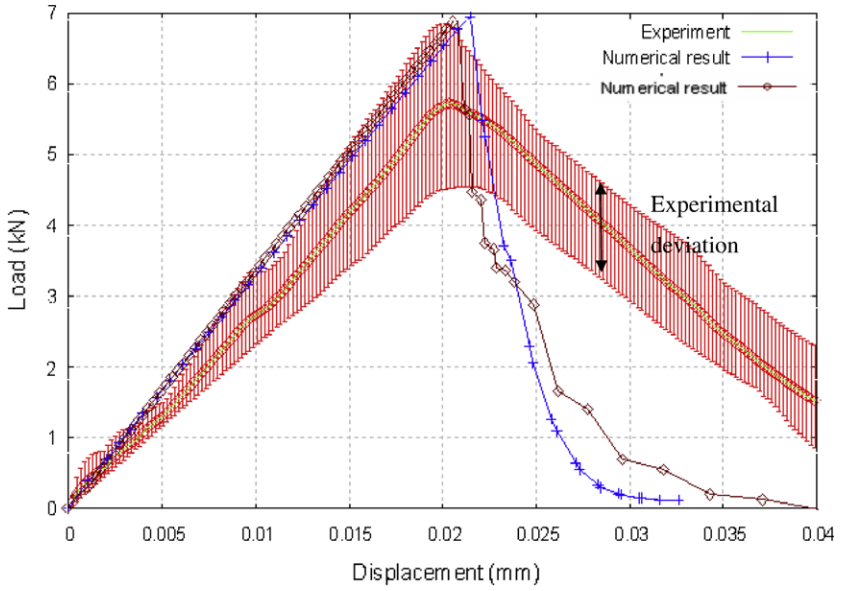

Fig. 10. Load–displacement curves for 3-point bending test on concrete.

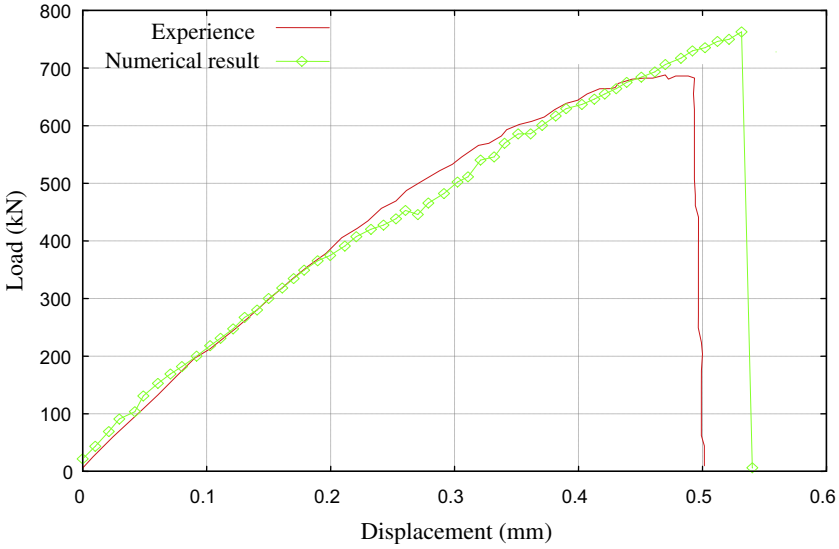

Fig. 11. Load–displacement curves for compression test.

Several reasons can explain the differences between the curves. The "kill element" technique used in the study is mesh-dependant and leads to a more abrupt post-peak part than in experiments. The contact between the tool and the sample is bilateral sticking; then frictional effects and progressive energy dissipation are not taken into account. The experimental instrumentation (displacement sensor under the load axis of the 3-point bending test) is also questionable since cracks start from this location.

3.2.4.2. Validation of the modelling. In order to validate this meso-modelling of mortar, a series of "Brazilian" splitting tests has been performed. A 16 × 32 cm cylinder is diametrically loaded in compression between two plates. The contact is correctly taken into account by the intermediary of two fine timber rods between the plates and the cylinder. For this test the particle size distribution is the same than for compression test.

Fig. 12 shows the geometry and the mesh used for the simulation. A bilateral sticking contact between the tool and the sample is

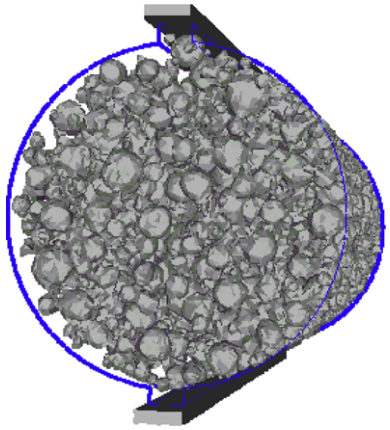

Fig. 12. "Brazilian" splitting test. Repartition of the aggregates in the sample.

imposed. The parallelepipedic parts above and under the cylinder simulate the timber rods and enable a better contact.

Fig. 13 presents the damage evolution in the sample volume according to the tool displacement. It can be noted that damage is not initiated at the center of the cylinder but at some distance. It confirms results obtained in 2D by Saouridis [25]. Then the damage reaches a critical value at the center of the sample, which generates cracks along the load axis.

The evaluation of the general displacement, based on data given by strain gages is relatively complex as it includes geometry of the sample and complex boundary conditions. This is the reason why stress–strain relationships are preferred. The theoretical link between the load peak and the maximum principal stress σ_I is obtained as follows:

$$\sigma_I = \frac{F_{max}}{\pi b R} \tag{12}$$

where b and R are respectively the length and the radius of the sample.

Fig. 14 presents the numerical stress–strain curve based on some points placed at the center of the sample and compared with the experimental curve. A good correlation not only for the maximal principal stress but also for the post-peak behaviour is obtained and enables to validate the mesoscale modelling.

4. Sensitivity analyses

4.1. Influence of aggregates repartition

The influence of the aggregates repartition on the global material response is first analyzed. Three concrete samples, with different random repartition of aggregates but with the same particle size distribution, are submitted to a 3-point bending test. The modelling is configured as described in Section 3.2.4. Fig. 15 shows the three load–displacement curves obtained. It can be noted that aggregates repartition does not really influence the global behaviour. It means also that all results presented in this paper can be generalized to all concrete samples with the same formulation.

4.2. Influence of aggregates volume

The influence of coarse aggregates volume on the concrete compressive strength is analyzed. The same model configuration than in Section 3.2.4 is used. Different meshes have been considered to generate the granular skeleton. The more there are aggregates to generate, the finer the mesh is. Table 8 shows the particle size distribution used for the different simulations and for 16 × 32 cm cylindrical concrete sample. At the bottom of the table, the volume of coarse aggregates is evaluated. Special attention is paid in order

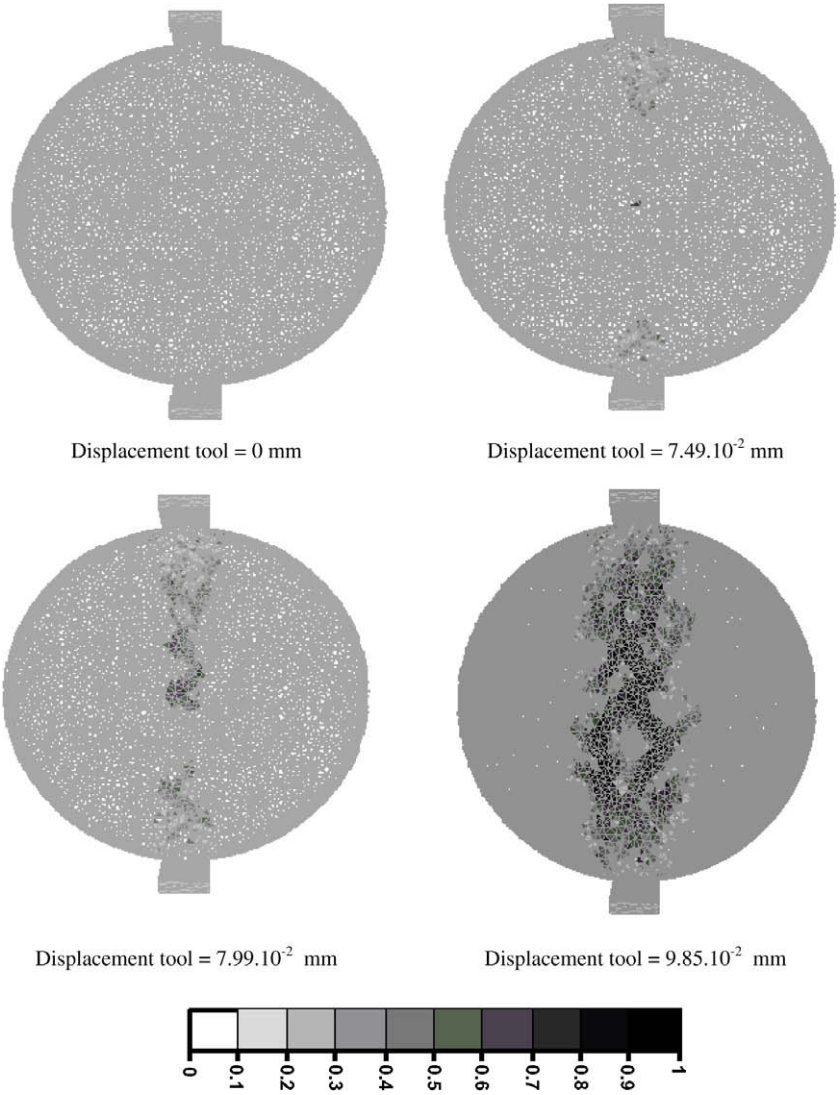

Fig. 13. Damage evolution for the "Brazilian" splitting test.

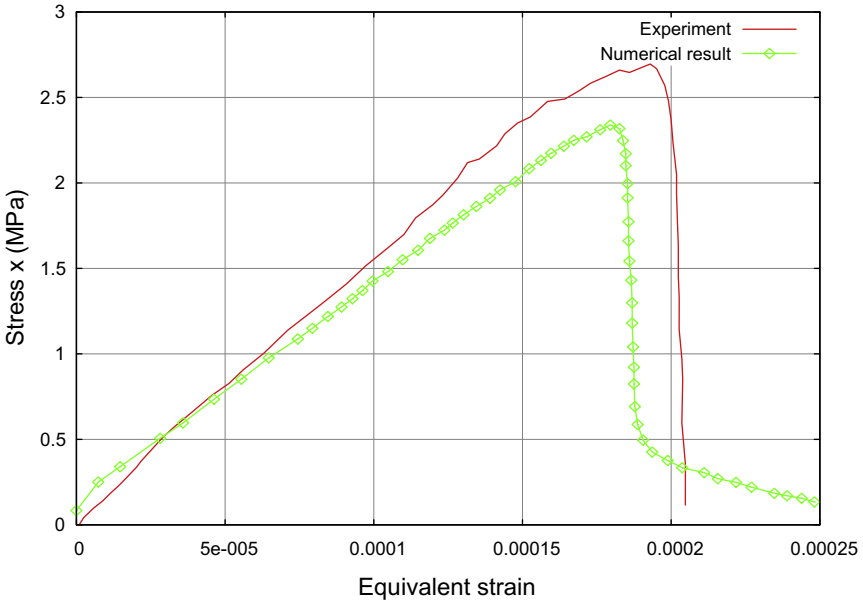

Fig. 14. Stress–strain curve for the "Brazilian" splitting test.

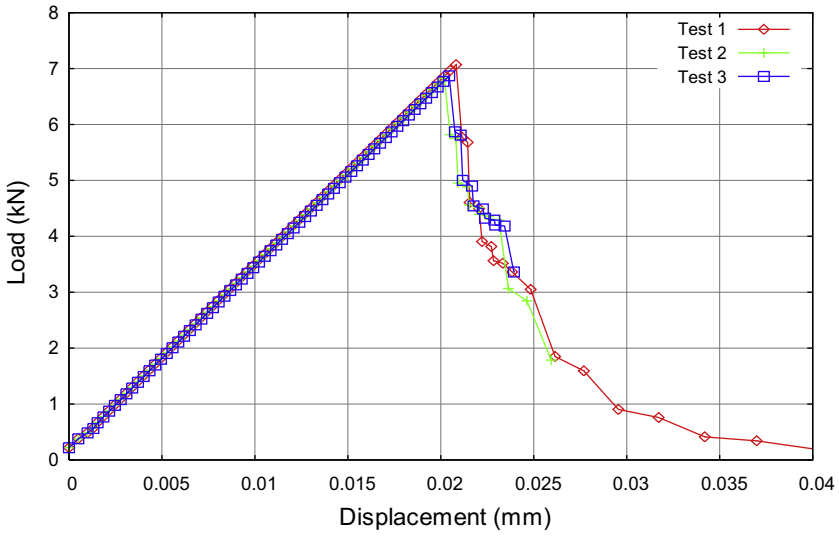

Fig. 15. Load–displacement curves with different aggregates repartition.

Table 8
Different particle size distribution.

Mean diameter (mm)	Number of aggregates				
22.5	40	40	40	40	40
18		294	294	294	294
14.25			502	502	502
11.25				428	428
9					604
7.15					1110
Total	40	334	836	1264	2978
Real coarse aggregate volume (%) in the sample	3.87	18.8	29.4	34.44	41.3
Real aggregate volume (%) in the sample (coarse aggregates and sand)	47.8	62.8	73.5	78.4	85.3

to differentiate this volume with the total grains volume for which sand content has to be taken into account. This last volume is then calculated from Table 3. That enables to determine the real grain volume in the sample (last line of Table 8).

The coarse aggregates volume increases from 3.5% to 40%, which corresponds at the end to a standard concrete (2978 aggregates in a 16 × 32 cm cylindrical concrete sample). The compressive strength according to the aggregates cumulative volume is then drawn in Fig. 16. The compressive strength remains constant up to 60%, and then increases significantly with the grain content. This result is in accordance with previous experimental works [26]. Further research is needed to determine the influence of the ITZ volume evolution implied by aggregates contents on the compressive strength.

4.3. Influence of aggregates maximal diameter

The numerical influence of the aggregates dimensions on the load–displacement curves for compression tests is analyzed in this section. The same model configuration than in previous paragraph is also considered. Table 9 shows the number of aggregates to gen-

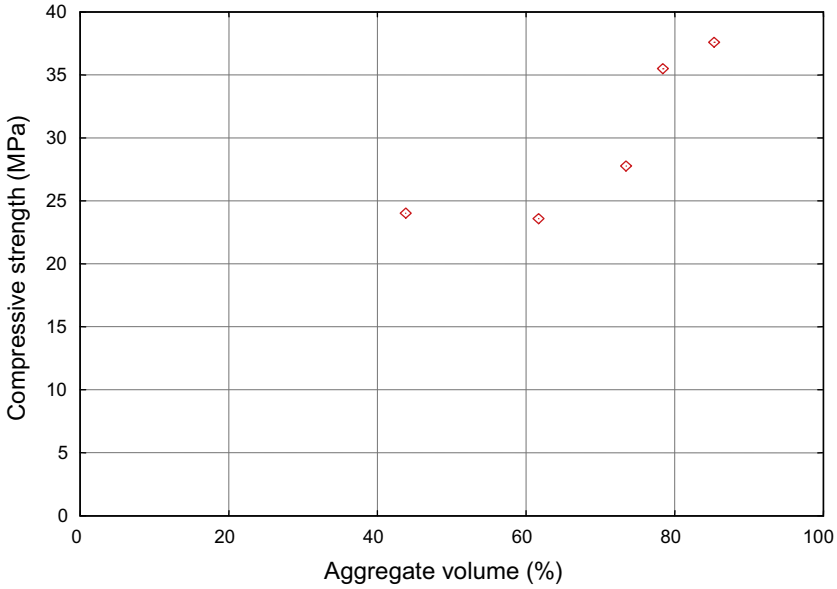

Fig. 16. Evolution of the compressive strength according the aggregates content in the sample.

Table 9
Particle size distribution for the same volume of generated aggregates.

Mean diameter (mm)	22.5	11.25	7.125
Number of aggregates	64	506	2000
$V_{aggregate}$ (mm^3)	383.8	377.57	378.7

erate in order to reach the same aggregates content. The repartition of the different granular skeletons in the 16 × 32 cm cylindrical concrete sample is shown in Fig. 17. The evolution of the compressive strength according to the aggregate maximal size is presented in Fig. 18. This figure shows that for this range of values, the aggregate diameter has little influence on strength. This result is in relative good accordance with previous experimental works [27]. In these former studies, it has been shown that the influence of the aggregates diameter depends on the W/C ratio. For high ratios (0.55 and 0.7) and for a specific concrete, no impact has been observed whereas for lower ratio (0.4 as in the present study) the strength falls slightly from 47 to 43 MPa in the considered diameter values.

However, further research is needed in order to determine the effect of the modification of the granular skeleton on the mechanical behaviour of mortar (evolution of ITZ volume and possible cracking due to shrinkage).

5. Application to alkali-silica reaction

5.1. ASR swelling mechanism

The mechanisms of the alkali-silica reaction have been described by many authors [28,29]. Many divergences appear concerning the role of each component in the swelling mechanism. More recently, experimental methodologies have been carried out to better understand the initiation and process of swelling [8,30–32]. A model describing the chemical reaction from microscale to macroscale has been developed by giving a relationship between concrete and granular skeleton swellings. The volume variation of the granular skeleton, put into evidence with these previous experimental works, is then used as an input data for the 3D computational tool developed in the present paper.

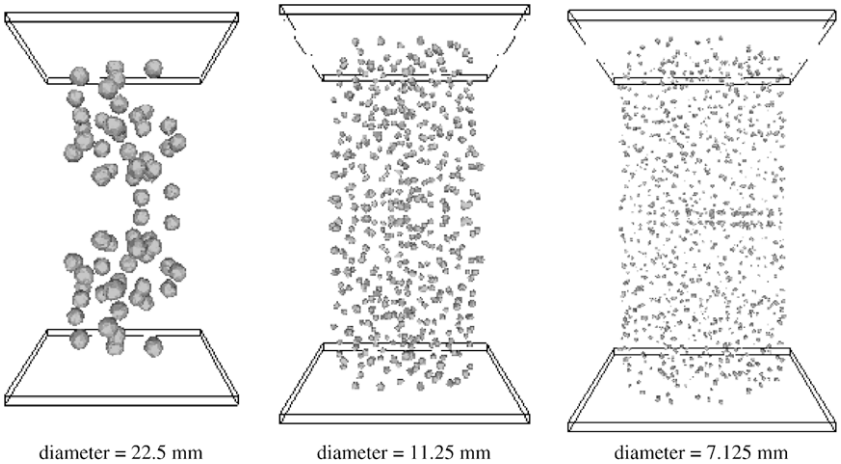

Fig. 17. Repartition of different granular skeletons in a concrete sample.

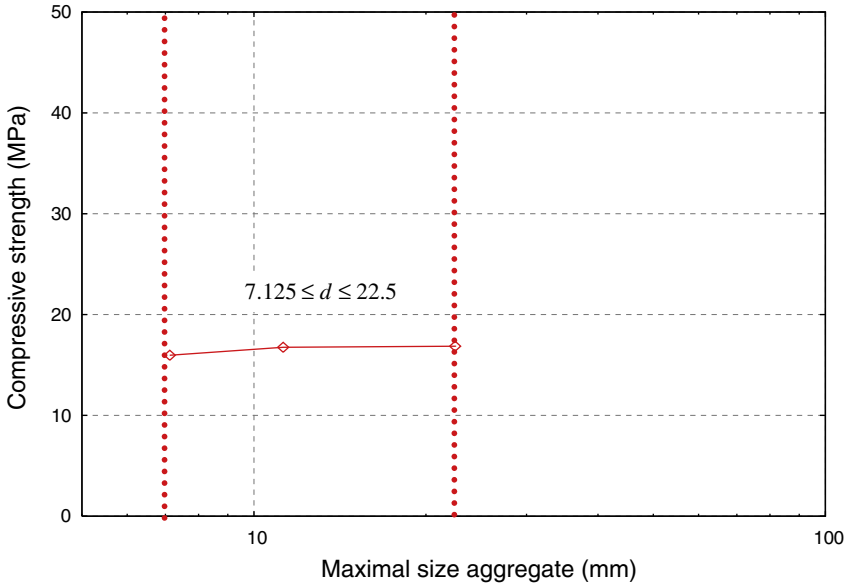

Fig. 18. Compressive strength according to aggregate maximal diameter.

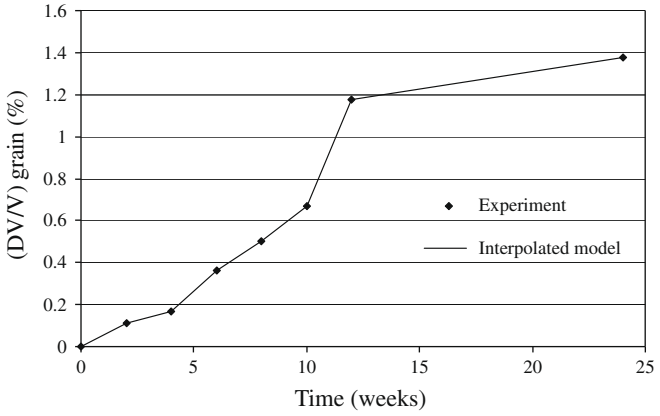

Fig. 19. Swelling curve of the grain versus time.

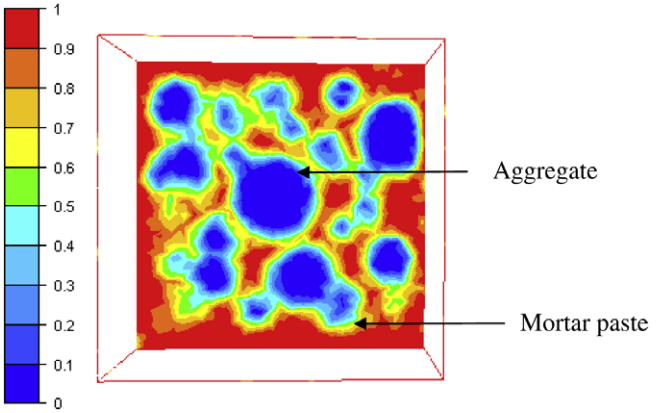

Fig. 21. Cuting plane in the sample submitted to the ASR – undamaged material corresponds to the aggregates.

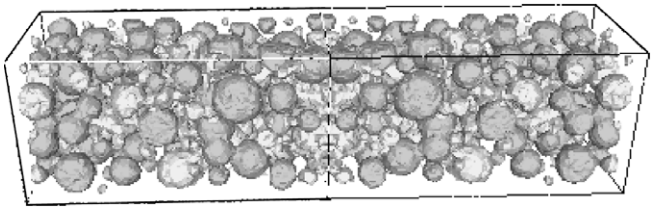

Fig. 20. Position of the reactive aggregates (in dark grey) into the aggregate skeleton.

5.2. Modelling of the consequences of ASR after seven days

5.2.1. Chemical–mechanical problem

The FE software used, as previously explained, is based on a velocity–pressure formulation. The constitutive equations have then been modified to take into account the pressure generated by the aggregates swelling. It is considered that the swelling of the aggregates is proportional to the reaction advancement ξ. If ξ is equal to zero no swelling appears, if ξ is equal to 1 the asymptotic swelling is reached. In this modelling, ξ corresponds to the experimental data given by the volume variation of the grains [31].

The strain tensor due to ASR is written as follows [33]:

$$\varepsilon_{ij}^{\mathrm{ASR}} = \xi \varepsilon^{\infty} \delta_{ij} \tag{13}$$

where ε^{∞} is the asymptotic strain for an aggregate swelling.

As the tensor $\varepsilon_{ij}^{\mathrm{ASR}}$ is purely spherical, it induces a supplementary term in the hydrostatic pressure to describe the swelling of the finite elements belonging to reactive aggregates.

Finally the general weak velocity–pressure formulation associated to the whole problem is given by (see also [33]):

$$\text{Find} \quad (v,p) \in V \times P$$
$$\begin{cases} \int_{\Omega} s(v) : \dot{\varepsilon}(v^*) d\Omega - \int_{\Omega} p \,\mathrm{div}(v^*) d\Omega - \int_{\partial\Omega} \tau_{\mathrm{imp}} \cdot v^* dS = 0 \\ \int_{\Omega} p^* [-\mathrm{div}(v) - \frac{\dot{p}}{\chi} + \frac{\dot{\chi}}{\chi^2} p + 3\varepsilon^{\infty} \dot{\zeta}] d\Omega = 0 \\ \forall (v^*, p^*]) \in V_0 \times P \end{cases} \tag{14}$$

Ω is the considered volume, and $\partial\Omega$ its boundary ($\partial\Omega_{\mathrm{v}}$ the surface in contact with the tools of the testing machine), τ_{imp} is a surface load applied to Ω on its boundary $\partial\Omega_{\tau} = \partial\Omega - \partial\Omega_{\mathrm{v}}$. s is the deviatoric part of the stress field, χ the compressibility modulus. V, V_0 and P are the following virtual fields:

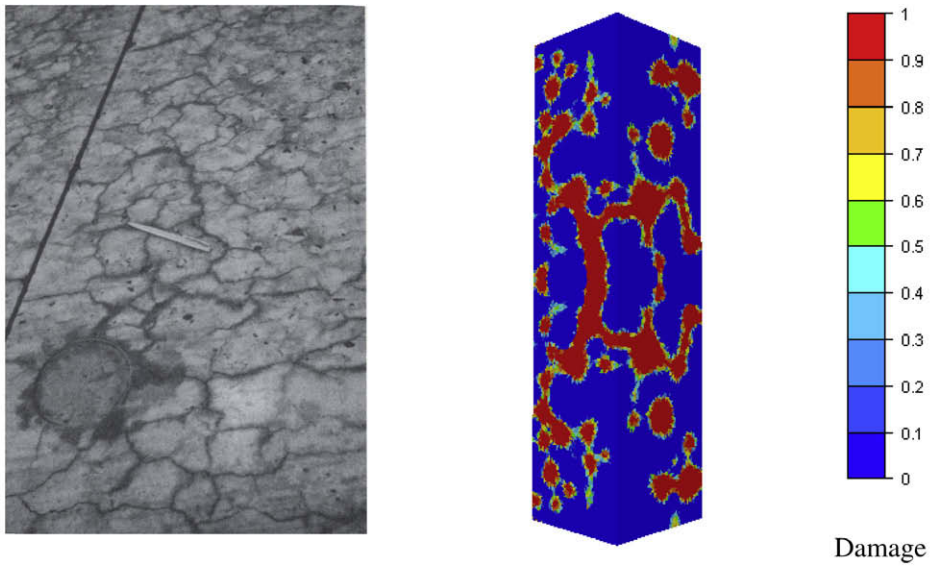

a) A portion of concrete road pavement, Cape Town. Length of the pencil is 125 mm. [34]

b) Damage evolution at the surface with the 3D numerical model

Fig. 22. Crack pattern developed at the surface of a concrete submitted to ASR. Comparison experimental–numerical results. (see above-mentioned references for further information).

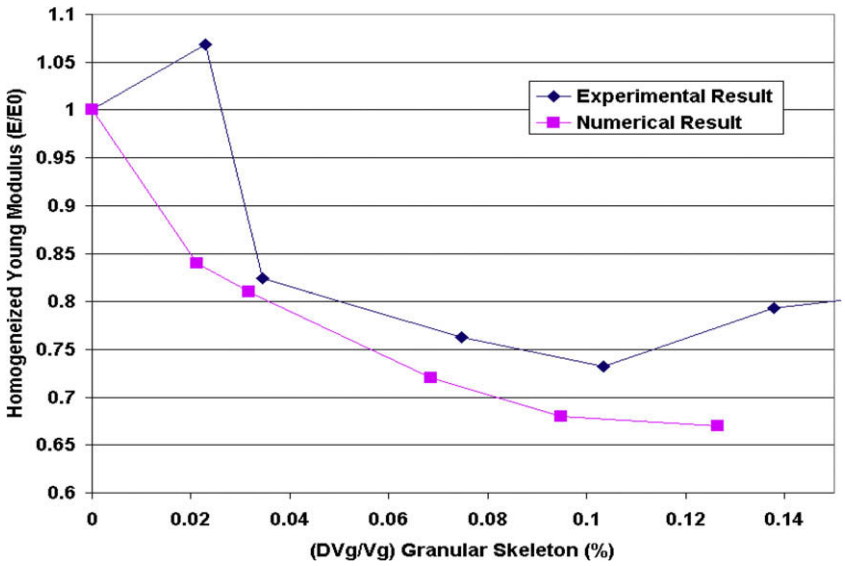

Fig. 23. Evolution of the homogenised Young's modulus according to skeleton expansion.

$$V = \{v, v \in \{H^1(\Omega)\}^3, (v - v_{\text{tool}}) \cdot n \leqslant 0 \quad \text{on} \quad \partial\Omega_v\}$$
$$V_0 = \{v, v \in \{H^1(\Omega)\}^3, v \cdot n \leqslant 0 \quad \text{on} \quad \partial\Omega_v\} \qquad (15)$$
$$P = L^2(\Omega)$$

$L^2(\Omega)$ is the space of the functions which are square integratable on Ω and H^1 is the Sobolev space of L^2 integratable functions.

In the mechanical contribution of each finite element to the local matrices some conditions intervene to distinguish the behaviour of a finite element belonging to the mortar or to the aggregates. Then a finite element of the mortar and the non-reactive aggregates has no chemical strain ($\xi = 0$) whereas a finite element of the aggregates has a purely elastic behaviour (the term $\frac{\dot{\chi}}{\chi^2} p$ is removed). A possible inelastic behaviour of aggregates is not considered in this work.

5.2.2. Input data: experimental results

The experimental results obtained by Dehaudt [8] on the present studied concrete submitted to ASR are used. These experiments have been carried out on $7 \times 7 \times 28$ cm parallelepipedic samples at 60 °C (controlled temperature) and 100% RH to accelerate the reaction. Concrete samples have been stored in autoclaves after seven days of hardening. This last point explains too why parameters identification and experimental campaign have been

led on 7 days maturated samples (Section 3). Nevertheless, the cure conditions lead to a modification of the initial conditions which cannot be taken into account at this moment, at this stage of the modelling.

Reaction degrees have been evaluated by Riche et al. [31] in order to measure the swelling of the aggregates skeleton. Fig. 19 presents the volume variation of the granular skeleton according to time.

This evolution constitutes the input data of the 3D mesomodelling. An interpolation is realized on these experimental values to obtain the volume variation of the grain at each time step.

5.2.3. Modelling of the mechanical consequences of ASR

For this simulation, as in experiments, only half of the aggregates are reactive. Fig. 20 shows the reactive aggregates among the whole granular skeleton. The choice of the reactive aggregates is completely random and is uniformly present for each grain size. The nature of the swelling is isotropic. The mesoscale model is configurated as previously presented (Section 3). Fig. 21 shows a cutting plane in the sample after 14 days of chemical reaction. Aggregates, in dark, are purely elastic and consequently totally undamaged. It can also be seen that damage tends to be more important when it reaches the sample faces.

This result is representative of what is observed in reality: whereas damage increases progressively inside, a cracking map at concrete surface is observed. Typically the crack pattern develops irregular polygonal forms. An example of this numerical cracking map is shown in Fig. 22.

The decrease of the Young's modulus can be evaluated with such a modelling. In order to reach this goal a compression test has been performed after various times of swelling. Fig. 23 presents the evolution of the ratio E/E_0 according to granular skeleton expansion. E_0 and E are, respectively, the Young's moduli of the sound and damaged concrete. The global decrease is correctly described by the numerical modelling. The differences at the beginning (experimental increase of the Young's modulus and numerical decrease) is probably due to the cement hardening after 7 days, phenomenon not taken into account in the modelling.

These results, close to experiments, validate once again the numerical mesoscopic approach.

6. Conclusion

This paper presents the development of a 3D mesoscale modelling of concrete behaviour. The material is here considered as a biphasic medium with coarse aggregates embedded in mortar. The algorithm generating grains in a concrete sample is largely described. It is based on a random generation of aggregates following the real particle size distribution. This description takes also into account physical aspects such as maximum paste thickness and edge effects.

In this simulation the non-local Mazars model is considered in order to reproduce the mortar behaviour whereas aggregates are supposed to be purely elastic. The complete parameters identification and validation are presented too. It has been shown that it is preferable to determine these various coefficients from experimental campaigns led on concrete samples rather than mortar samples. This secondary but interesting result is a consequence of the apparition of interfacial transition zones around coarse aggregates and cracking due to shrinkage phenomenon. This last point has to be taken into account in multi-scale studies which aim at reproducing concrete behaviour starting from its microstructure and progressively up-scaling the various outcomes to higher levels.

The two last paragraphs concern the applications of the mesoscale modelling. First, sensitivity studies are performed: the influence of aggregates repartition, volume and maximal diameter is analyzed. The obtained results seem to be in agreement with former experimental works. It is then shown that in the considered range of values, compressive strength is linked to aggregates content. On the contrary, aggregates repartition and maximal diameter seem to have little influence on the global mechanical behaviour. Finally the mechanical consequences of alkali-silica reaction are simulated. The approach is based on an isotropic dilatation phenomenon of reactive aggregates shown previously by Bulteel et al. [30]. The 3D numerical tool succeeds in reproducing not only crack pattern on concrete faces but also the progressive loss of material stiffness with a certain accuracy.

Acknowledgements

This work has been supported by ATILH. We would like to express our appreciation for this support. We also gratefully acknowledge the members of the following committee of Isabelle Comby-Peyrot's PhD thesis for valuable comments.

References

[1] O. Bernard, F.J. Ulm, E. Lemarchand, Cement and Concrete Research 33 (2003) 1293–1309.
[2] P. Rossi, X. Wu, Magazine of Concrete Research 44 (161) (1992) 271–280.
[3] F. Grondin, H. Dumontet, A. Ben Hamida, G. Mounajed, H. Boussa, Cement and Concrete Research 37 (2007) 1453–1462.
[4] J. Wang, Development and Application of a Micromechanics-based Numerical Approach for the Study of Crack Propagation in Concrete, EPFL, Lausanne (Switzerland), PhD Thesis, 1994.
[5] J.P.B. Leite, V. Slowik, J. Apel, Computers and Structures 85 (2007) 1293–1303.
[6] P. Wriggers, S.O. Moftah, Finite Elements in Analysis and Design 42 (2006) 623–636.
[7] F. Dupray, Y. Malecot, L. Daudeville, E. Buzaud, A mesoscopic model for the behaviour of concrete under high confinement, International Journal for Numerical and Analytical Methods in Geomechanics, in press, published online in Wiley InterScience.
[8] S. Dehaudt, Etude de la Dégradation D'un Béton Soumis à la Réaction Alcali-granulat, Ecole des Mines de Douai, Douai (France), PhD Thesis, 2002 (in French).
[9] D.N. Arnold, F. Brezzi, M. Fortin, Calcolo 21 (1984) 337–344.
[10] E. Schlangen, J.G.M. Van Mier, Materials and Structures 25 (1992) 534–542.
[11] G. Mounajed, Exploitation du Nouveau Modèle, Béton Numérique dans Symphonie, Concept, Homogénéisation du Comportement Thermomécanique des BHP et Simulation de L'endommagement Thermique Cahiers du CSTB, 2002 (in French).
[12] F.H. Wittmann, H. Sadouki, T. Steiger, Experimental and numerical study of effective properties of composite materials, in: C. Huet (Ed.), Micromechanics of Concrete and Cementitious Composites, Universitaires Romandes Lausanne, 1993, pp. 59–82.
[13] F. De Larrard, Concrete Mixture-proportioning – A Scientific Approach, Modern Concrete Technology Series 9, E&FN SPON, London, 1999.
[14] A. Caquot, Le rôle des matériaux inertes dans le béton, Mémoires de la Société des Ingénieurs Civils de France (1937) 562–592 (in French).
[15] J. Mazars, Application de la Mécanique de L'endommagement au Comportement Non Linéaire et à la Rupture du Béton de Structure, Univ. Paris VI (France), Thèse de Doctorat d'état, 1984 (in French).
[16] G. Pijaudier-Cabot, Z.P. Bazant, ASCE Journal of Engineering Mechanics 113 (1997) 1512–1533.
[17] J. Mazars, Engineering Fracture Mechanics 25 (5–6) (1986) 729–737.
[18] R.H.J. Peerlings, R. de Borst, W.A.M. Brekelmans, J.H.P. de Vree, International Journal for Numerical Methods in Engineering 39 (1996) 3391–3403.
[19] L. Jason, Relation Endommagement Perméabilité Pour les Bétons, Applications Aux Calculs de Structures, Ecole Centrale de Nantes, France, PhD Thesis, 2004 (in French).
[20] I. Comby, P.O. Bouchard, F. Bay, F. Bernard, E. Garcia-Diaz, Computational Materials Science 40 (3) (2007) 327–340.
[21] I. Rechenberg, Evolutionsstragegie: Optimierung Technischer Systeme Nach Prinziepen der Biologischen Evolution, Stuttgart, 1973.
[22] J. Bisschop, J.G.M. van Mier, Cement and Concrete Research 32 (2) (2002) 279–287.
[23] T. Akçaoglu, M. Tokyay, T. Çelik, Cement and Concrete Research 35 (2) (2005) 358–363.
[24] F. Bernard, S. Kamali-Bernard, W. Prince, Cement and Concrete Research 38 (2008) 449–458.

[25] C. Saouridis, Identification et Numérisation Objectives des Comportements Adoucissants – Approche Multiéchelle de L'endommagement du Béton, Ecole Normale Supérieure de Cachan, France, PhD Thesis, 1988 (in French).
[26] A.F. Stock, D.J. Hannant, R.I.T. Williams, Magazine of Concrete Research 31 (1979) 225–233.
[27] W.A. Cordon, H.A. Gillepsie, Journal of the American Concrete Institute 60 (8) (1963) 1029–1052.
[28] L.S. Dent-Glasser, N. Kataoka, Cement and Concrete Research 11 (1) (1981) 1–9.
[29] S. Chatterji, P. Christensen, Cement and Concrete Research 20 (2) (1990) 285–290.
[30] D. Bulteel, E. Garcia-Diaz, J.M. Siwak, C. Vernet, H. Zanni, Alkali-aggregate reaction: a method to quantify the reaction degree, in: Proceedings of the 11th International Conference on AAR in Concrete, Quebec, Canada, 2000, pp. 11–20.
[31] J. Riche, E. Garcia-Diaz, D. Bulteel, J.M. Siwak, Mechanism of damage for the alkali-silica reaction: relationship between swelling and reaction degree, in: R. Dhir, M. Roderick Jones, Zheng Li (Eds.), Repair, Rejuvenation and Enhancement of Concrete, Proceedings of International Conference of Dundee, 2002, pp. 94–102.
[32] E. Garcia-Diaz, J. Riche, D. Bulteel, J.-M. Siwak, C. Vernet, Cement and Concrete Research 36 (2) (2006) 395–400.
[33] I. Comby-Peyrot, Development and Validation of a 3D Computational Tool to Describe Damage and Fracture due to Alkali-silica Reaction in Concrete Structures, Ecole des Mines de Paris, Sophia-Antipolis, France, PhD Thesis, 2006.
[34] R.N. Swamy (Ed.), The Alkali-aggregate Reaction in Concrete, Blackie, London, 1992.